

RESEARCH ARTICLE SUMMARY

HUBBARD MODEL

Origin and fate of the pseudogap in the doped Hubbard model

Fedor Šimkovic IV*, Riccardo Rossi, Antoine Georges, Michel Ferrero

INTRODUCTION: Large systems of interacting quantum particles host a wealth of collective phenomena, such as superconductivity, magnetism, and metal-insulator transitions. Prominent examples are materials with strong correlations between electrons, such as transition metal oxides and twisted bilayer graphene, and ultracold atomic gases trapped in optical lattices. Understanding these systems is a formidable theoretical and computational challenge, with implications both for fundamental physics and for the design of new functional materials. One of the unusual states of matter observed in these systems is the so-called “pseudogap” regime in which the electronic excitations of a metal are suppressed in a selective manner depending on their momentum. A central open question is whether such a peculiar state can exist down to low temperature without intervening long-range orders being formed.

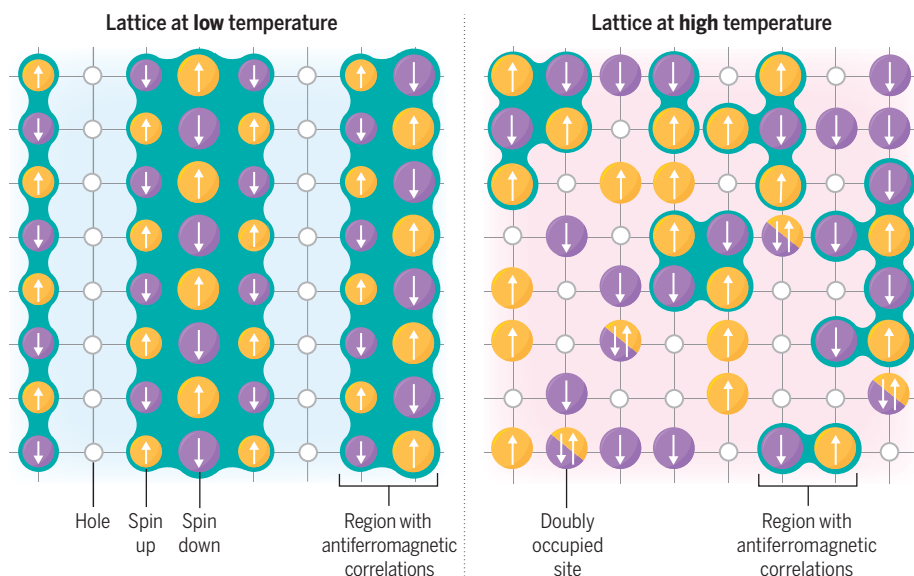
RATIONALE: The Fermi-Hubbard model, introduced in 1963, established itself as a fun-

damental theoretical platform to investigate interacting quantum systems. Despite its formal simplicity, it may be capable of capturing the essence of strongly correlated materials. In the absence of an analytical solution, it has been the subject of numerous computational studies, but it still eludes a controlled solution in its most notable regimes at finite temperature. The main obstacles come from the exponentially large size of the configuration space and the so-called fermionic sign problem that most algorithms suffer from, hence impeding the simulation of large systems. In this work, we used a state-of-the-art unbiased computational algorithm, diagrammatic Monte Carlo, to obtain controlled results in nontrivial regimes of the Fermi-Hubbard model on an infinite two-dimensional square lattice. We provide answers to some outstanding questions regarding the origin and fate of the pseudogap state as temperature is lowered for a broad range of values of the model parameters. We benchmark our results against several other

numerical methods, including dynamical mean-field theory and its cluster extensions.

RESULTS: Our calculations identified three distinct physical regimes as a function of temperature and electronic density: a weakly correlated metal, a strongly correlated metal, and a pseudogap regime. The formation of the pseudogap is associated with the onset of antiferromagnetic spin correlations. At weak coupling, they are long ranged, whereas their spatial extent becomes shorter at strong coupling. As these correlations develop, a deformation of the Fermi surface is first observed at intermediate densities in the strongly correlated metal. At densities closer to one electron per site, the coherence of electronic excitations for “antinodal” momenta close to the Brillouin zone boundary is suppressed, and a pseudogap appears. In this regime, the self-energy that quantifies the modification of the dispersion and lifetime of electronic excitations by interactions develops a quasi-pole. We show how spin fluctuation theory can be modified to provide a good description of the nonlocal part of the self-energy both in the weak and strong coupling regimes. In contrast to spin correlations, we did not observe the development of sizable charge correlations associated with the pseudogap in the temperature regimes accessible to our method. We addressed the fate of the pseudogap at low temperature by performing an extrapolation of the pseudogap region to zero temperature. We show that the range of density and coupling strength where a pseudogap is found in this limit precisely coincides with that in which ground-state studies find a stripe phase with long-range spin and charge order.

CONCLUSION: We have obtained controlled results that highlight the crucial role of spin correlations in driving the formation of the pseudogap. Eventually, this state becomes unstable and, in the absence of a next-nearest-neighbor hopping, turns into a stripe phase. This result and the corresponding handshake between finite and zero-temperature methods is a major achievement of our work. We have further demonstrated the robustness of our findings by investigating the pseudogap for a nonzero next-nearest-neighbor hopping and have observed a similar finite-temperature behavior. In this case, further work involving controlled ground-state studies will be necessary to clarify the fate of the pseudogap at low temperature, which remains an outstanding question. ■



The low-doping regime of the Hubbard model with nearest-neighbor hopping. At low temperature (left), the system is stripe ordered. There are large regions where the spins are antiferromagnetically organized. The holes form vertical bands between these regions. As the temperature is increased (right), the long-range order is lost, and the pseudogap regime appears. Regions with antiferromagnetic correlations are present in a homogeneous background of disordered holes and doubly occupied sites.

The list of author affiliations is available in the full article online.

*Corresponding author. Email: fsmkovic@gmail.com

Cite this article as F. Šimkovic IV *et al.*, *Science* **385**, eade9194 (2024). DOI: 10.1126/science.ade9194

S READ THE FULL ARTICLE AT
<https://doi.org/10.1126/science.ade9194>

RESEARCH ARTICLE

HUBBARD MODEL

Origin and fate of the pseudogap in the doped Hubbard model

Fedor Šimkovic^{1,2,*}, Riccardo Rossi^{3,4}, Antoine Georges^{1,2,5,6}, Michel Ferrero^{1,2}

The relationship between the pseudogap and underlying ground-state phases has not yet been rigorously established. We investigated the doped two-dimensional Hubbard model at finite temperature using controlled diagrammatic Monte Carlo calculations, allowing for the computation of spectral properties in the infinite-size limit and with arbitrary momentum resolution. We found three distinct regimes as a function of doping and interaction strength: a weakly correlated metal, a correlated metal with strong interaction effects, and a pseudogap regime at low doping. We show that the pseudogap forms both at weak coupling, when the magnetic correlation length is large, and at strong coupling, when it is shorter. As the temperature goes to zero, the pseudogap regime extrapolates precisely to the ordered stripe phase found by ground-state methods.

Materials in which electrons are strongly interdependent, ranging from transition metal oxides to twisted bilayer graphene, display notable collective phenomena, such as high-temperature superconductivity or metal-insulator transitions (1). This physics has highlighted the relevance of the program outlined by Dirac in 1929 (2), namely, the need to develop practical methods of calculating and predicting the properties of large quantum systems of interacting particles. In this context, the Hubbard model (3, 4) quickly established itself (5) as a fundamental and paradigmatic model that, although not fully realistic on a microscopic level, may capture the essence of the “strong correlation” problem. Moreover, analog platforms, such as cold atoms in optical lattices, provide a highly controllable realization of the Hubbard model (6).

At an electronic density of one electron per site, the Hubbard model can host an insulating phase in which charge motion is blocked by strong repulsive interactions: a Mott insulator. Understanding the nature of the metallic phase obtained when doping this insulator with charge carriers is a fundamental question with broad relevance. In two dimensions, several studies (3, 7) have established that the metallic state at low doping levels is highly unconventional: At elevated temperature, it displays a partial destruction of the Fermi surface associated with the formation of a

“pseudogap,” corresponding to a depletion of the density of excited states available to the system. This pseudogap state has been experimentally observed in high-temperature copper-oxide superconductors (cuprates) (8). At low temperature, a rich diversity of phases with different kinds of intertwined long-range order—most notably, charge density waves—has been numerically predicted (9). This raises the central and still widely open question: Is the pseudogap state a fundamentally distinct kind of metallic state that could, in principle, be stabilized down to zero temperature without encountering an ordering instability, or is it a finite-temperature intermediate state that is always unstable to various kinds of long-range ordering?

Interrogating the Hubbard model about this fundamental question has proven to be a daunting challenge. In recent years, substantial progress has been made in understanding the physical properties of this model through the development and use of controlled and accurate computational methods, most of which fall into two groups. Wave function-based methods have addressed the nature of the ground state and have demonstrated that it is characterized by spin and charge ordering, forming stripe patterns at low doping levels (10–12), as proposed early on in the context of mean-field studies (13–15). Methods aimed at nonzero temperatures have revealed that the Hubbard model hosts a pseudogap regime associated with magnetic correlations (7, 16–23). Understanding the fate of the pseudogap state as temperature is lowered and how it connects to ground states with long-range order calls for a “handshake” between different families of established computational methods and the development of new ones.

In this work, we provide an answer to some of these outstanding questions. Using an un-

biased computational method, we identified the crossovers between the different regimes of the two-dimensional Hubbard model. We show that the pseudogap originates from magnetic correlations and, by following its temperature dependence, we provide evidence that it eventually evolves into a ground state with long-range spin and charge stripe order.

We studied the doped repulsive two-dimensional Hubbard model defined by $\hat{H} = \sum_{\mathbf{k}, \sigma} \epsilon_{\mathbf{k}} \hat{c}_{\mathbf{k}\sigma}^\dagger \hat{c}_{\mathbf{k}\sigma} + U \sum_{\mathbf{r}} \hat{n}_{\mathbf{r}\uparrow} \hat{n}_{\mathbf{r}\downarrow} - \mu \sum_{\mathbf{r}, \sigma} \hat{n}_{\mathbf{r}\sigma}$ with $\epsilon_{\mathbf{k}} = -2t(\cos k_x + \cos k_y)$. Here, $\hat{c}_{\mathbf{k}\sigma}^\dagger$ ($\hat{c}_{\mathbf{k}\sigma}$) creates (annihilates) a fermion with momentum \mathbf{k} and spin σ , $\hat{n}_{\mathbf{r}\sigma}$ is the (spin-) number operator at lattice site \mathbf{r} , μ is the chemical potential, and U the on-site interaction strength. We also performed computations with a non-zero next-nearest-neighbor hopping, t' ; see below and in (24). We investigated the temperature range $0.07t \leq T \leq 0.25t$ and coupling strengths up to $U = 8.5t$. We used diagrammatic Monte Carlo, which is an unbiased, numerically exact technique formulated directly in the thermodynamic limit (22, 25–30). It allowed us to obtain physical quantities with arbitrary momentum resolution, which is a crucial advance over other available methods for the purposes of this study. We also compared our results with dynamical mean-field theory (31), its 16-site dynamical cluster approximation extension (16–18, 20), and continuous-time quantum Monte Carlo (CT-INT) (24, 32, 33). In the following work, the hopping amplitude t is used as the unit of energy and temperature.

Finite temperature phase diagram and crossovers

By analyzing our data, we identified in Fig. 1 three distinct physical regimes separated by well-defined crossovers as a function of interaction strength $U \leq 8$ and hole-doping levels up to $\delta = 1 - n = 20\%$, with n being the average electronic density per site. The five panels in Fig. 1 display how these crossovers evolved as a function of temperature $T = \{0.07, 0.1, 0.15, 0.2, 0.25\}$. We describe these regimes here in qualitative terms; see (24) for details.

The first regime (blue regions, Fig. 1) corresponds to a weakly correlated metal. We identified the Fermi surface (FS) from the maximum of the spectral function proxy $A(\mathbf{k}) = -\frac{1}{\pi} \text{Im}G(\mathbf{k}, i\omega_0)$, where $\omega_0 = \pi T$ is the lowest Matsubara frequency, $\omega_p = (2p + 1)\pi T$ (34). In this regime, the FS is electron-like and very close to that of the noninteracting system. The spectral weight is uniform along the FS and relatively large, the self-energy is rather small, and quasiparticles are long-lived. This regime is found at large doping levels or weak interactions, a representative point being W in Fig. 1.

For stronger interactions and intermediate doping levels, a different metallic regime (green regions) was found in which the topology of

¹CPHT, CNRS, Ecole Polytechnique, Institut Polytechnique de Paris, 91128 Palaiseau, France. ²Collège de France, 11 place Marcelin Berthelot, 75005 Paris, France. ³Institute of Physics, École Polytechnique Fédérale de Lausanne (EPFL), CH-1015 Lausanne, Switzerland. ⁴LPTMC, CNRS, Sorbonne Université, 4 place Jussieu, F-75005 Paris, France. ⁵Center for Computational Quantum Physics, Flatiron Institute, 162 Fifth Avenue, New York, NY 10010, USA. ⁶DQMP, Université de Genève, 24 quai Ernest Ansermet, CH-1211 Genève, Suisse. *Corresponding author. Email: fsmkovic@gmail.com

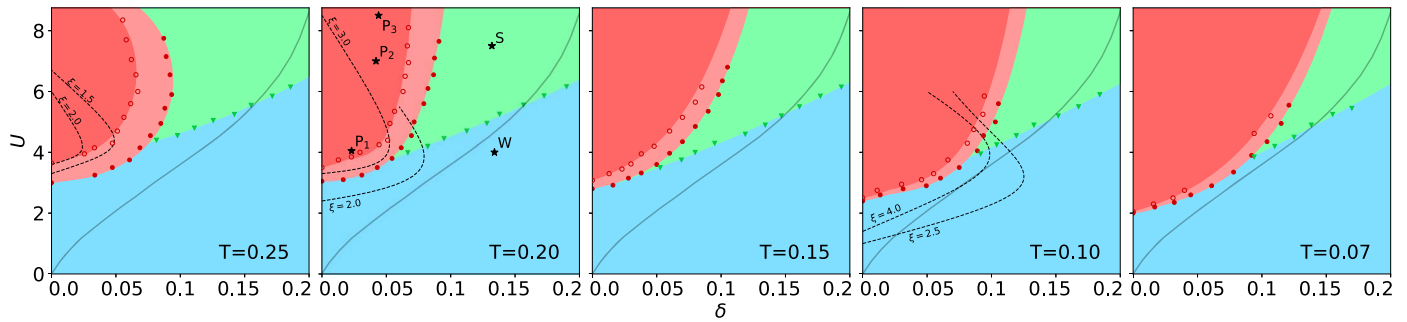


Fig. 1. Distinct regimes of the Hubbard model. The five panels show their evolution as a function of temperature from Diagrammatic Monte Carlo. The blue and green regions correspond to a weakly and strongly correlated metal, respectively. The red regions correspond to the regime where a pseudogap is present, with light red indicating the onset of the PG opening in the antinodal region, and dark red

indicating a regime with a fully open pseudogap. Dashed lines indicate contours of constant spin correlation length ξ . Symbols (open red circles, filled red circles, and green triangles) are explained in detail in the text. The full gray line, reproduced from (9), indicates the region where the ground state displays long-range spin or charge stripe ordering. For details on calculations, see (24).

the FS is hole-like. The system undergoes an interaction-driven Lifshitz transition when crossing into this regime from the weakly correlated metal, as indicated by the green triangles in Fig. 1. The self-energy becomes relatively large, and the quasiparticle lifetime decreases significantly. We refer to this regime as a strongly correlated metal (representative point, S).

The red regions of Fig. 1 are characterized by a pseudogap, which we detected by multiple criteria based on the spectral function, self-energy, and uniform susceptibility, as discussed in detail in (24). The boundary of the lighter red region indicates the opening of the pseudogap at the antinode. It then gradually spreads in momentum space through a series of momentum-selective crossovers, the darker red region indicating the regime where the pseudogap is fully formed. In agreement with earlier studies (7), the pseudogap at strong and intermediate coupling always emerges out of a metallic state, which has a hole-like FS topology. Comparing the different panels in Fig. 1, the pseudogap regime is seen to become more extended as temperature is lowered.

To address the important question of the interplay between the spatial range of magnetic correlations and the formation of the pseudogap, we depict in Fig. 1 contour lines of equal spin correlation length ξ (dashed black lines). It is seen that, at weak interactions, the pseudogap is associated with fairly long-ranged spin correlations (35, 36). By contrast, at stronger coupling, a pseudogap is already found at a high temperature, when the correlation length is only a couple of lattice sites. This is a key qualitative difference between the nature of the pseudogap regime at weaker (representative point P_1) and stronger coupling (P_2 and P_3). Other differences between these two regimes of the pseudogap are further described below.

The nature of spin correlations actually undergoes a qualitative change from commensu-

rate [$\mathbf{q} = (\pi, \pi)$] at low doping and higher temperature to incommensurate [$\mathbf{q} = (q, \pi)$] at higher doping and lower temperature, in agreement with the findings of previous studies (37–39). For $T = 0.2$, the crossover happens around 10% doping, whereas at $T = 0.1$, roughly 7.5% is sufficient (and very weakly dependent on U). At these intermediate temperatures, the onset of the pseudogap is not directly sensitive to the commensurate or incommensurate nature of magnetic correlations.

Fingerprints of crossovers between regimes

In Fig. 2, we present momentum-resolved spectral properties over a quarter of the Brillouin zone (BZ) at $T = 0.2$ for selected points in the phase diagram of Fig. 1 corresponding to the different physical regimes. In the left column, we display the low-energy spectral function proxy $A(\mathbf{k})$. The middle column represents the imaginary part of the self-energy at the lowest Matsubara frequency $\text{Im}\Sigma(\mathbf{k}, i\omega_0)$, whereas the right column shows the slope of the imaginary part of the self-energy obtained from the first two Matsubara frequencies, $\Delta\text{Im}\Sigma(\mathbf{k}) \equiv \text{Im}\Sigma(\mathbf{k}, i\omega_0) - \text{Im}\Sigma(\mathbf{k}, i\omega_1)$. In a conventional metallic phase, this quantity is positive. We have chosen a momentum resolution of 64×64 for all quantities.

The top row (W) of Fig. 2 corresponds to the weakly correlated metal ($U = 4$, $n = 0.866$). The Fermi surface obtained from the maximum of $A(\mathbf{k})$ in the BZ (green line) essentially coincides with that of the noninteracting system (white line, middle column). It is also very close to the zero-energy quasiparticle line obtained from $\epsilon_{\mathbf{k}} - \mu + \text{Re}\Sigma(\mathbf{k}, i\omega_0) = 0$ (black line), which indicates the expected FS if the lifetime effects coming from the imaginary part of the self-energy were neglected. The fact that it is close to the interacting FS is consistent with the rather small and mostly uniform self-energy in this regime. The spectral weight along the whole FS is large and essentially uniform in this regime.

The second row (S) corresponds to a strongly correlated metal at intermediate doping ($U = 7.5$, $n = 0.868$). The momentum dependence of $\text{Re}\Sigma(\mathbf{k}, i\omega_0)$ induces a reshaping of the zero-energy quasiparticle line that becomes hole-like. The FS is also hole-like, in strong contrast to that of the noninteracting system, but its location does not quite coincide with that of the zero-energy quasiparticle line because the imaginary part of the self-energy has prominent features close to $(\pi, \pi/2)$. Lifetime effects suppress the antinodal spectral weight by about 9% with respect to the node. The change of FS topology from electron-like to hole-like can be interpreted as a correlation-induced Lifshitz transition and is shown with green dots in Fig. 1. For both regimes S and W , $\Delta\text{Im}\Sigma(\mathbf{k})$ is positive over the whole BZ, compatible with a metallic behavior.

The third row (P_1) is characteristic of a weak-coupling pseudogap ($U = 4$, $n = 0.977$). Similarly to the case above, the real part of the self-energy shifts the zero-energy quasiparticle line to a hole-like shape. However, as the maxima in the imaginary part have moved closer to $(\pi, 0)$, the interacting FS actually remains electron-like, and the antinodal spectral weight is further reduced to roughly 13% as compared with the node. As temperature is decreased, the antinodal spectral weight is reduced, confirming the presence of a pseudogap.

The last row (P_2) displays a pseudogap with more pronounced features and located deeper inside the strong-coupling regime ($U = 7$, $n = 0.977$). Quasiparticles are short lived, with a Fermi arc forming around the nodal region, and the antinode spectral intensity is reduced by about 14%. As in the weak-coupling pseudogap, the zero-energy quasiparticle line is strongly modified and hole-like. Lifetime effects strongly suppress the spectral weight above the antiferromagnetic Brillouin zone, and the maxima of the spectral function define an electron-like FS. For both P_1 and P_2 , the slope of the self-energy is negative in a region just above the

antiferromagnetic BZ. As shown in more detail in (24), this quantity is a good indicator of the onset of the pseudogap region, which commences when the slope changes sign close to the antinode (full red circles, Fig. 2). As the doping is decreased, the area of the Brillouin zone where the slope changes sign extends out of the antinodal region into the nodal region (open red circles, Fig. 1) (24).

It is notable that, as temperature is decreased in the pseudogap region, the imaginary part of the self-energy increases, although the momentum space region where it is large remains outside the antiferromagnetic BZ (24). As a result, the lifetime effects get stronger with decreasing temperature at the antinode, whereas they have a much weaker effect at the node, where quasiparticles remain quite coherent. This dichotomy between antinodal and nodal quasiparticles is also observed in cluster extensions of dynamical mean-field theory (DMFT) (17, 20, 40–42).

We have also performed computations with a nonzero value of the next-nearest-neighbor hopping t' , as detailed in figs. S19 and S20. Our results suggest that the mechanism for the opening of the PG as well as the crossovers reported above are generic.

Relating numerical results to a modified spin fluctuation theory

In this section, we ask whether the PG regime can be described by some form of spin-fluctuation theory. It is known from past work (35, 36, 43) that this is indeed the case at weak coupling. The question is whether such a description is also possible at strong coupling despite the rather short correlation length that invalidates the conditions for a conventional application of spin fluctuation theory. We note that previous work based on a “fluctuation diagnostics” (44) in the framework of both cluster extensions of DMFT (21) and diagrammatic MC (22) has shown that the formation of the PG has indeed originated from sizeable short-ranged spin correlations. This point was further reinforced by a direct evaluation of the spin and charge susceptibilities in both the weak- and the strong-coupling PG region. These quantities are displayed in Fig. 3 [see also (37)] and indicate that the physics is dominated by spin fluctuations in the temperature regime that we investigated, whereas the charge response is, by contrast, very weak. This points at the pseudogap being of magnetic origin rather than being caused by the fluctuations of a low-temperature charge order, which is also consistent with the conclusions from cluster extensions of DMFT. These considerations provide a strong incentive for attempting a spin fluctuation-inspired description of the PG.

To this end, we divided the self-energy into a local (uniform in momentum space) and non-local part: $\Sigma = \Sigma_{\text{loc}} + \Sigma_{\text{nl}}$. The local part is quite

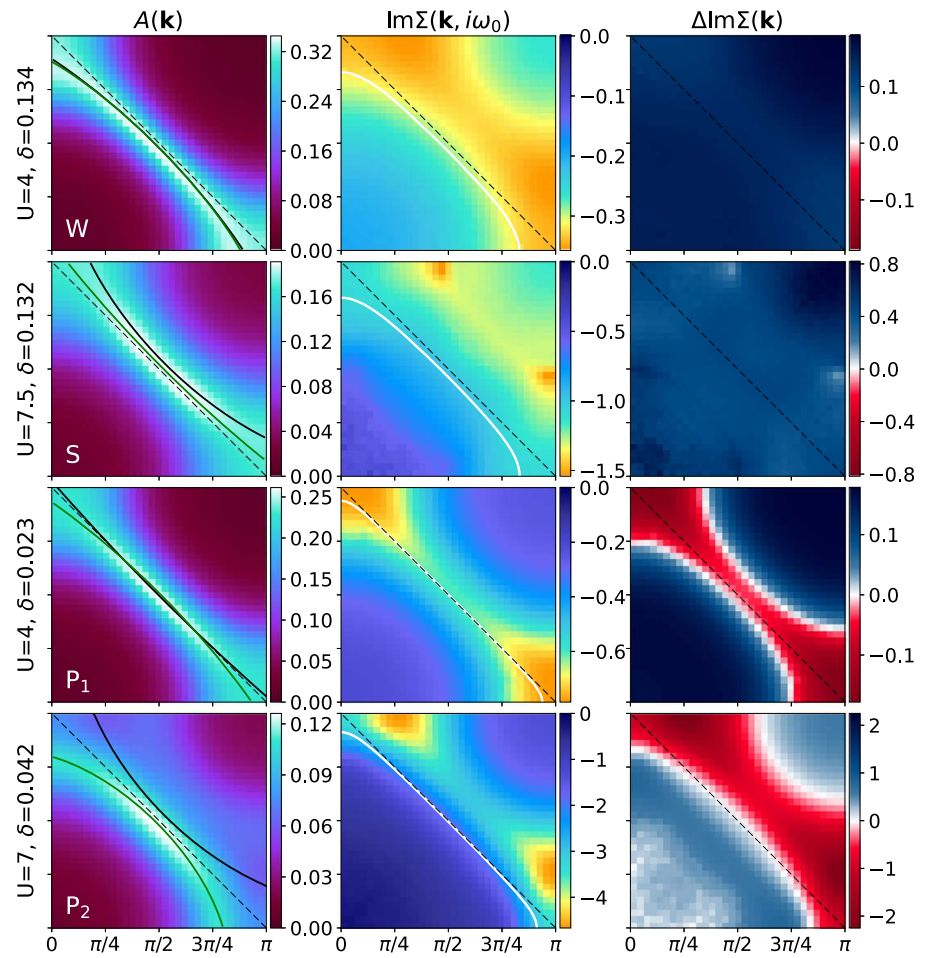


Fig. 2. Fingerprints of the different regimes. The momentum-resolved spectral function, $A(\mathbf{k})$ (left); the imaginary part of the self-energy, $\text{Im} \Sigma(\mathbf{k}, i\omega_0)$ (middle); and the difference between the imaginary part of the self-energy at the two lowest Matsubara frequencies, $\Delta \text{Im} \Sigma(\mathbf{k}) = \text{Im} \Sigma(\mathbf{k}, i\omega_0) - \text{Im} \Sigma(\mathbf{k}, i\omega_1)$ (right) are shown for selected points W, S, P_1 , and P_2 in the phase diagram of Fig. 1 at temperature $T = 0.2$. Results obtained using Diagrammatic Monte Carlo data are displayed for $\mathbf{k} = (k_x, k_y)$ in the upper right quarter of the BZ. The white lines indicate the noninteracting Fermi surface. The green lines show the maximum of the spectral function. The zero-energy quasiparticle lines are shown in black.

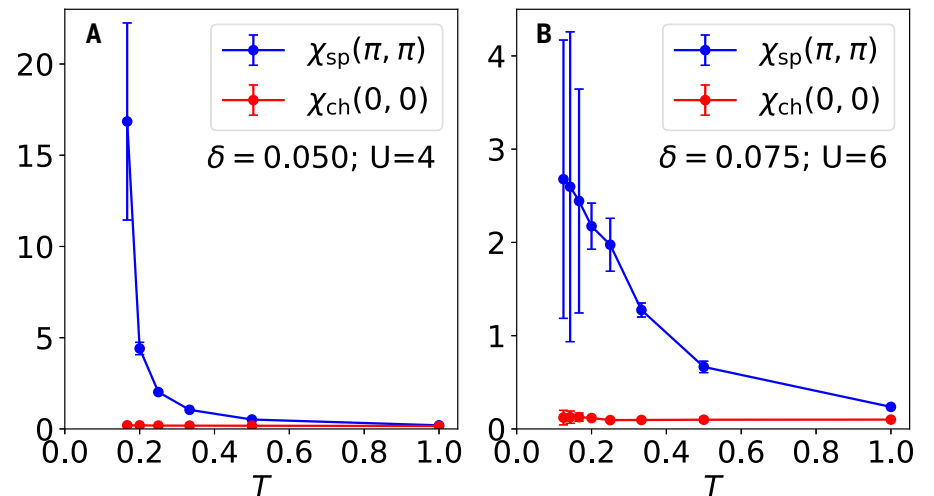


Fig. 3. Spin and charge correlations. The zero-frequency spin and charge susceptibilities at their maximum value in momentum space (obtained by Diagrammatic Monte Carlo) are displayed as a function of temperature for representative examples of the (A) weak- and (B) strong-coupling pseudogap regimes.

large, especially in the strong-coupling regime, and is not adequately approximated by spin fluctuation theory. In (24), we assessed the accuracy of DMFT in computing the local component. For the nonlocal component, we drew inspiration from Hedin's equation (45) $\Sigma = -G \star W \star \Gamma$ involving convolutional products over momenta and frequencies, with $W = U - U^2 \chi_{\text{sp}}$. Here, Γ is the vertex function, and χ_{sp} is the dynamical spin susceptibility. We approximated this exact expression by considering the following ansatz for the nonlocal part of the self-energy:

$$\Sigma_{\text{nl}}^{\text{sp}}(\mathbf{k}, i\omega_0) = \bar{\gamma} U^2 T \frac{1}{N} \sum_{\mathbf{q}} \frac{G_0(\mathbf{k} + \mathbf{q}, i\omega_0, \bar{\mu})}{(\pi - q)^2 + \bar{\xi}^{-2}} \quad (1)$$

Here, we have replaced the vertex Γ by a constant $\bar{\gamma}$ and the effective spin interaction W by an Ornstein-Zernike form of the commensurate spin susceptibility χ_{sp} centered around $\pi = (\pi, \pi)$ and with correlation length $\bar{\xi}$. In Eq. 1, we used a noninteracting form of the Green's function G_0 that, notably, involves an adjustable chemical potential $\bar{\mu}$. Furthermore, we have limited the frequency convolution to the zero bosonic Matsubara frequency only, an approximation that is known to become more accurate at low temperature when a pseudogap opens (35, 43). We used a fitting procedure on our numerically exact data in order to determine the three parameters, $\bar{\gamma}$, $\bar{\mu}$, and $\bar{\xi}$, and consider only the imaginary part of the self-energy in the optimization process. In Fig. 4, we present the real and imaginary parts of the nonlocal self-energy for three different points within the pseudogap regime, comparing our numerically exact results to the optimized spin-fluctuation expression.

The first column of Fig. 4 shows an example of the weak-coupling pseudogap regime (P_1 : $U = 4$, $n = 0.977$). Here, we found agreement between the self-energy fit and the original data both for the real and the imaginary part. The momentum and overall magnitude of the fit is close to perfect. The parameter $\bar{\mu} = -0.26$ is somewhat lower than the noninteracting chemical potential corresponding to the density ($\mu_0 = -0.10$). The parameter $\bar{\xi} = 5.0$ is close to the actual (commensurate) value of $\xi = 4.3$ obtained numerically. Lastly, $\bar{\gamma} = 0.5$ hints at the fact that the Γ vertex is relatively uniform and not very large.

The middle column corresponds to a point in the strong-coupling pseudogap regime (P_2 : $U = 7$, $n = 0.958$). Our spin fluctuation ansatz still produced a qualitatively correct picture, but differences are apparent at the quantitative level. The extrema in the imaginary part are in the correct location but are somewhat broader than in the data. We emphasize that adjusting $\bar{\mu}$ is essential to correctly place the extrema of $\text{Im}\Sigma$ (white lines, Fig. 4). Using such

a freedom for the noninteracting starting point is indeed often used to improve perturbative expansions (22, 33, 37, 46–48). The fitting procedure yields $\bar{\mu} = -0.89$, $\bar{\xi} = 1.60$ (we expected the exact value to be $\xi \lesssim 2$), and $\bar{\gamma} = 4.90$, which points to the fact that the vertex Γ becomes large in this regime. Notably, the real part has the correct momentum structure, but because our fitting procedure for $\bar{\gamma}$ only considers the imaginary part, the overall magnitude of the real part is roughly four times too large. The fact that a single consistent value of $\bar{\gamma}$ cannot be found to fit both the imaginary and real parts of the self-energy points to a strong momentum and/or frequency dependence of the vertex Γ . The right column of Fig. 4 has the same density and an even larger coupling strength (P_3 : $U = 8.5$, $n = 0.956$). From fitting the self-energy, we observed a continuation of the trend found at lower U , where $\bar{\mu} = -1.03$, $\bar{\xi} = 1.25$, and $\bar{\gamma} = 4.84$.

A properly modified spin-fluctuation theory provides an excellent theoretical description of the nonlocal part of the self-energy in the weak-coupling pseudogap regime and still does qualitatively well in its strong-coupling counterpart. In the latter regime, however, a quantitative fit of the imaginary and real parts cannot be simultaneously achieved. Amending our ansatz by the possibility of an incommensurate χ_{sp} with maxima at $\mathbf{q} = (\pi \pm \delta, \pi)$ does not improve the fitting procedure. The authors of (23) made the interesting observation that the vertex became complex at strong coupling and proposed that this may be a key to understanding the PG at strong coupling in a spin fluctuation framework. However, we found that allowing for a complex phase $\bar{\gamma} = \bar{\gamma}_0 e^{i\kappa}$ with the idea of mixing contributions from the real and imaginary self-energies does not actually lead to a better fit. These observations point to the importance of the

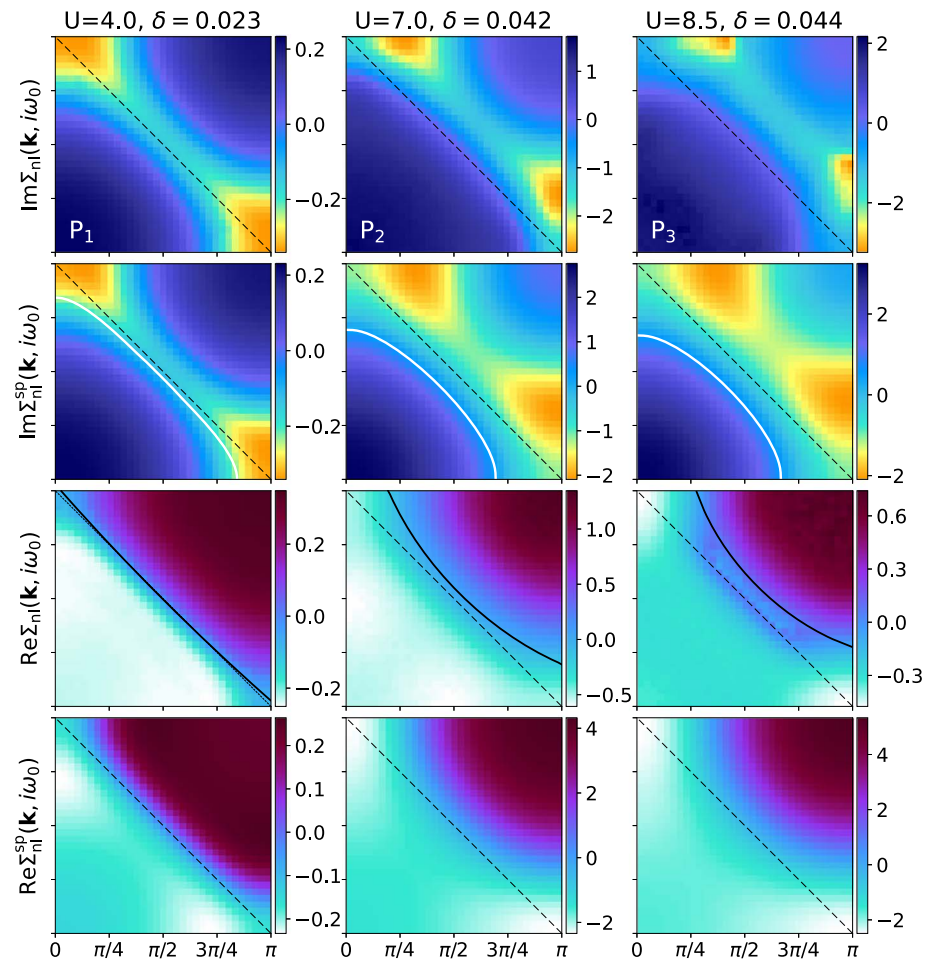


Fig. 4. Comparison to modified spin fluctuation theory. Momentum-resolved nonlocal components of the real (bottom two rows) and imaginary (top two rows) parts of the self-energy are shown for selected points within the pseudogap regime at $T = 0.2$. The numerically exact results obtained by Diagrammatic Monte Carlo and displayed for $\mathbf{k} = (k_x, k_y)$ in the upper right quarter of the BZ (first and third rows) are compared to a spin fluctuation theory fitting procedure (second and fourth rows), as described in the text. Black lines indicate the zero-energy quasiparticle lines. White lines indicate the FS associated with the bare Green's function $G_0(k, i\omega_0 = i\pi T, \bar{\mu})$ used in the fits.

momentum and frequency dependence of the vertex function in the strong-coupling regime. We also note that using the interacting Green's function G within our ansatz (in the spirit of self-consistent or bold perturbation theory) instead of a noninteracting G_0 (with an adjustable $\bar{\mu}$) yields much poorer fits (35, 43).

The fate of the pseudogap at low temperature: Handshake with ground-state methods

A major open issue in relation to the doped Hubbard model is the connection between the physical nature of the ground state and that of finite temperature crossovers. Distinct sets of computational methods have been successfully used in investigating separately these questions (3, 4), but a handshake between these approaches is still mostly lacking. In the present context, an outstanding question remains on what happens to the pseudogap regime upon cooling toward $T = 0$. Does charge and/or spin ordering take place? Do the Fermi arcs observed at high temperature eventually evolve into a reconstruction of the Fermi surface at low temperature? These questions have also been the subject of intense debate and experimental investigations in the context of cuprates (49). In this work, we make progress toward such a handshake by performing an extrapolation toward $T = 0$ of the crossovers found above at finite temperature and by comparing to a recent ground-state study (9).

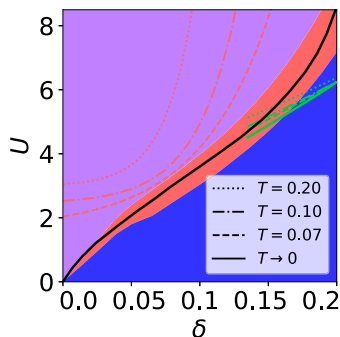


Fig. 5. Fate of the pseudogap at low temperature. By extrapolating to $T = 0$ the pseudogap crossover at different temperatures indicated in the figure (dotted, dash-dotted, and dashed red lines), we estimated the boundary (red region) separating the low-doping regime with a pseudogap to the higher-doping regime without a pseudogap (the width of the region reflects the error bars of the extrapolation). This boundary was found to coincide within error bars to the phase transition line reported in (9) (black line), which separates ground states with (purple) and without (blue) spin and charge stripe ordering. The green line indicates the low-temperature extrapolation of the Lifshitz transition line.

In Fig. 5, we show the results of an extrapolation down to $T = 0$ of our numerically exact finite T results for the position of the various crossovers (fig. S12). The full red region in Fig. 5 indicates the extrapolated $T = 0$ boundary between the region with (purple) and without a PG (blue). The $T = 0$ extrapolation of the FS topology (Lifshitz) crossover coincides with the PG boundary up to a doping level of around 13.5% and deviates from it at higher doping. The full black line in Fig. 5 is adapted from (9). It represents the ground state phase transition between a phase with long-range spin and charge stripe order (10, 11, 13–14) and a phase at higher doping levels with only short-range spin and/or charge correlations. This boundary was computed by auxiliary field quantum Monte Carlo, and the results are in good agreement with those of multiple separate studies with other methods (50, 51). Notably, our result for the extrapolated pseudogap boundary is in very good agreement with this phase transition line. This provides evidence that the pseudogap regime eventually becomes stripe ordered at zero temperature. This is one of the major conclusions of our work and addresses the long-standing question of the fate of the pseudogap regime as temperature is lowered toward the ground state.

Discussion and outlook

In Fig. 6, we present a sketch of the proposed strong-coupling phase diagram as a function of temperature and doping level. The pseu-

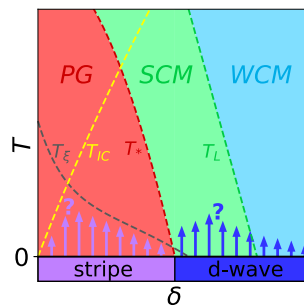


Fig. 6. Proposed unifying picture at strong coupling.

This schematic strong coupling phase diagram as a function of temperature and doping indicates the pseudogap (red, PG) and the strongly (green, SCM) and weakly correlated (blue, WCM) metallic regimes discussed in the text. The dashed gray and yellow lines refer to spin physics: Below the former (T_E), the magnetic correlation length exceeds a specified value, whereas below the latter (T_{IC}), the magnetic correlations become incommensurate. The ground state is a spin- and charge-ordered stripe state at low doping (purple region) and a superconductor at higher doping (blue region). These two zero-temperature phases are likely to extend to finite temperature in a manner that is not yet fully understood, as represented by arrows and question marks.

dop and Lifshitz crossovers from Fig. 5 are indicated by T^* and T_L . Additionally, we display the commensurate to incommensurate spin fluctuation crossover, T_{IC} , and the crossover from a short to a long spin correlation length, T_E , which were identified in (37). As established in previous work (12, 37) and also shown above, charge correlations only pick up at much lower temperatures. This implies that the formation of the pseudogap is driven by spin correlations, consistent with the conclusions from cluster extensions of DMFT (17, 20, 40–42). Charge correlations are, however, a necessary ingredient for the stripe ordering that was established to exist in the ground state (9, 50, 52). We postulate that charge correlations develop only once incommensurate spin correlations have grown to be sufficiently long ranged (Fig. 5). Very recently, strong indications that charge long-range (or quasi-long-range) order indeed takes place through a phase transition at a low nonzero temperature were obtained (53). From our data, we identified the ideal region of parameters to further investigate this question to be $n \sim 0.9$ and $U \sim 4$. Incidentally, this is where we experienced most difficulties with the resummation of perturbative series from diagrammatic Monte Carlo.

As doping is further increased, the stripe order eventually ceases to exist in the ground state. In the weak to intermediate coupling regime and in the absence of other instabilities, the Hubbard model will eventually turn superconducting because of the Kohn-Luttinger effect (54), albeit at possibly very low temperatures. For $U \leq 4$, it has been established that this instability is of the $d_{x^2-y^2}$ type up to 40% doping (55, 56). At stronger coupling, it has been shown that stripe ordering wins over superconductivity over a significant range of parameter space in the absence of next-nearest-neighbor hopping (51). The situation at doping levels just above the critical value at which stripe order disappears is still under investigation, but recent results seem to suggest that strong-coupling superconductivity exists over some range of doping (49, 50). Finite-temperature studies using approximate methods have also found d -wave superconductivity to exist in the vicinity of the pseudogap crossover (57, 58), and recent work supports that strong-coupling d -wave superconductivity is stabilized by a nonzero next-nearest-neighbor hopping t' (59). More work is needed to provide conclusive results about the critical temperature and doping extension of this phase.

Several extensions of our work are warranted. These include (i) extending the applicability of our approach to lower temperature and (ii), notably, extending the results presented in (24) for $t' \neq 0$ to a broader range of parameters and generalizing the handshake with ground-state methods to that case. These extensions

will require overcoming further computational challenges.

Methods

We consider thermal-equilibrium properties at temperature T in the grand-canonical ensemble with chemical potential μ , and we denote by $\langle \hat{O} \rangle$ the thermal average of an operator \hat{O} :

$$\langle \hat{O} \rangle \equiv \frac{\text{Tr}(\hat{O})e^{-\hat{H}'/T}}{\text{Tr}e^{-\hat{H}'/T}} \quad (2)$$

Here, $\hat{H}' = \hat{H} - \mu \sum_{r,\sigma} \hat{n}_{r\sigma}$ is the grand-canonical Hamiltonian. To compute dynamical quantities, we used the Matsubara formalism and the imaginary-time Heisenberg representation $\hat{O}(\tau) \equiv e^{\tau \hat{H}'} \hat{O} e^{-\tau \hat{H}'}$ of an operator $\langle \hat{O} \rangle$. The one-particle Green's function G in the Matsubara representation is:

$$G(\mathbf{k}, i\omega_n) \equiv - \int_0^{1/T} d\tau e^{i\omega_n \tau} \langle \hat{c}_{\mathbf{k}}(\tau) \hat{c}_{\mathbf{k}}^\dagger \rangle \quad (3)$$

Here, $\omega_n = (2n + 1)\pi T$ is a fermionic Matsubara frequency. It is possible to express G in terms of the spectral function $A(\mathbf{k}, \omega)$ by

$$G(\mathbf{k}, i\omega_n) \equiv - \int_{-\infty}^{\infty} d\omega \frac{A(\mathbf{k}, \omega)}{i\omega_n - \omega} \quad (4)$$

We define the zero-energy spectral function proxy $A(\mathbf{k})$ as

$$A(\mathbf{k}) \equiv -\frac{1}{\pi} \text{Im} G(\mathbf{k}, i\pi T) \quad (5),$$

which is a valid approximation of $A(\mathbf{k}, \omega = 0)$ at low-enough temperature. The self-energy Σ can be introduced from the Dyson's equation

$$\Sigma(\mathbf{k}, i\omega_n) \equiv [G_0(\mathbf{k}, i\omega_n)]^{-1} - [G(\mathbf{k}, i\omega_n)]^{-1}$$

Here, G_0 is the noninteracting Green's function. The static real-space spin and charge susceptibilities are defined as

$$\chi_{\text{sp}}(\mathbf{r}) \equiv \int_0^{1/T} d\tau \langle \hat{S}_z(\mathbf{r}, \tau) \hat{S}_z(\mathbf{r}, 0) \rangle \quad (7)$$

$$\chi_{\text{ch}}(\mathbf{r}) \equiv \int_0^{1/T} d\tau \langle \hat{n}(\mathbf{r}, \tau) \hat{n}(\mathbf{r}, 0) \rangle \quad (8)$$

Here, $\hat{S}_z(\mathbf{r}) \equiv \frac{1}{2}(\hat{n}_{\mathbf{r}\uparrow} - \hat{n}_{\mathbf{r}\downarrow})$ and $\delta \hat{n}(\mathbf{r}) \equiv \sum_{\sigma} (\hat{n}_{\mathbf{r}\sigma} - \langle \hat{n}_{\mathbf{r}\sigma} \rangle)$. From the Fourier transform of $\chi_{\text{sp}}(\mathbf{r})$, we can obtain an estimate of the magnetic correlation length ξ by fitting with a double-Lorentzian Ornstein-Zernike form (with constant offset):

$$\chi_{\text{sp}}(\mathbf{q}) \approx a \left(\frac{1}{|\mathbf{q} - (Q_x, Q_y)|^2 + \xi^2} + \frac{1}{|\mathbf{q} - (Q_y, Q_x)|^2 + \xi^2} \right) \quad (9)$$

We performed a numerical study of the Hubbard model by means of a version of Connected Determinant Diagrammatic Monte Carlo

(CDet) algorithm (28), which allows the calculation of high-order diagrammatic contributions to any (imaginary-time) physical quantity for arbitrary system sizes. This gave us access to numerically controlled results and fine momentum-space resolution.

We computed bare (corresponding to Feynman diagrams containing noninteracting Green's functions) double interaction-chemical-potential expansions in terms of the interaction strength U and a chemical-potential shift αU , as introduced in (37). We wrote any quantity of interest, \mathcal{O} , as an explicit function of the chemical potential μ and the interaction strength $\mathcal{O}(\mu, U)$. From $\mathcal{O}(\mu, U)$, we introduced two auxiliary mathematical quantities, including the Hartree expansion:

$$\begin{aligned} \mathcal{O}_{\text{Hartree}}(\mu_0, U) &\equiv \mathcal{O}\left(\mu_0 + U \frac{n_0}{2}, U\right) \\ &= \sum_{k=0}^{\infty} U^k \mathcal{O}_{\text{Hartree};k}(\mu_0) \end{aligned} \quad (10)$$

where n_0 is the number of particles per site at $U = 0$, and the double expansion:

$$\begin{aligned} \mathcal{O}_{\text{Double}}(\mu_0, \alpha, U) &\equiv \mathcal{O}(\mu_0 + \alpha U, U) \\ &= \sum_{k=0}^{\infty} \sum_{j=0}^k U^k \alpha^j \mathcal{O}_{\text{Double};k,j}(\mu_0) \end{aligned} \quad (11)$$

Diagrammatically, with respect to the bare series, the Hartree series does not contain any tadpole insertions, whereas the double series contains arbitrary chemical potential insertions. The calculation of $\mathcal{O}_{\text{Hartree};k}$ was performed using the algorithm of (28), whereas for obtaining $\mathcal{O}_{\text{Double};k,j}$, we used the method of (37). For the self-energy, we made use of a slightly modified algorithm compared with previous realizations (60–62), which we detailed for completeness in (24). We used a fast principal minor algorithm for the simultaneous evaluation of an exponential number of determinants (63) and the Many Configuration Markov Chain Monte Carlo for numerical integration (64). We chose the chemical potential shift αU that fixes the average particle number to a constant as a function of U . Jointly using this expansion with that of (10) provides us with a way to double-check the final result. It is well known (65) that for fermions on a lattice at finite temperature, the perturbative series has a nonzero radius of convergence. When outside the radius of convergence, we resummed the series by means of Padé approximants (61).

REFERENCES AND NOTES

1. M. Imada, A. Fujimori, Y. Tokura, Metal-insulator transitions. *Rev. Mod. Phys.* **70**, 1039–1263 (1998). doi: [10.1103/RevModPhys.70.1039](#)
2. P. A. M. Dirac, Quantum mechanics of many-electron systems. *Proc. R. Soc. Lond. A Math. Phys. Sci.* **123**, 714–733 (1929). doi: [10.1098/rspa.1929.0094](#)

3. M. Qin, T. Schäfer, S. Andergassen, P. Corboz, E. Gull, The Hubbard Model: A Computational Perspective. *Annu. Rev. Condens. Matter Phys.* **13**, 275–302 (2022). doi: [10.1146/annurev-conmatphys-090921-033948](#)
4. D. P. Arovas, E. Berg, S. A. Kivelson, S. Raghu, The Hubbard Model. *Annu. Rev. Condens. Matter Phys.* **13**, 239–274 (2022). doi: [10.1146/annurev-conmatphys-031620-102024](#)
5. P. W. Anderson, The Resonating Valence Bond State in La_2CuO_4 and Superconductivity. *Science* **235**, 1196–1198 (1987). doi: [10.1126/science.235.4793.1196](#); pmid: [17818979](#)
6. C. Gross, I. Bloch, Quantum simulations with ultracold atoms in optical lattices. *Science* **357**, 995–1001 (2017). doi: [10.1126/science.aal3837](#); pmid: [28883070](#)
7. W. Wu *et al.*, Pseudogap and Fermi-Surface Topology in the Two-Dimensional Hubbard Model. *Phys. Rev. X* **8**, 021048 (2018). doi: [10.1103/PhysRevX.8.021048](#)
8. J. G. Bednorz, K. A. Müller, Possible high T_c superconductivity in the Ba-La-Cu-O system. *Z. Phys. B Condensed Matter* **64**, 189–193 (1986). doi: [10.1007/BF01303701](#)
9. H. Xu, H. Shi, E. Vitali, M. Qin, S. Zhang, Stripes and spin-density waves in the doped two-dimensional Hubbard model: Ground state phase diagram. *Phys. Rev. Res.* **4**, 013239 (2022). doi: [10.1103/PhysRevResearch.4.013239](#)
10. S. R. White, D. J. Scalapino, Density Matrix Renormalization Group Study of the Striped Phase in the 2D t - J Model. *Phys. Rev. Lett.* **80**, 1272–1275 (1998). doi: [10.1103/PhysRevLett.80.1272](#)
11. Y.-F. Jiang, J. Zaanen, T. P. Devereaux, H.-C. Jiang, Ground state phase diagram of the doped Hubbard model on the four-leg cylinder. *Phys. Rev. Res.* **2**, 033073 (2020). doi: [10.1103/PhysRevResearch.2.033073](#)
12. A. Wietek, Y.-Y. He, S. R. White, A. Georges, E. M. Stoudenmire, Stripes, Antiferromagnetism, and the Pseudogap in the Doped Hubbard Model at Finite Temperature. *Phys. Rev. X* **11**, 031007 (2021). doi: [10.1103/PhysRevX.11.031007](#)
13. J. Zaanen, O. Gunnarsson, Charged magnetic domain lines and the magnetism of high- T_c oxides. *Phys. Rev. B Condens. Matter* **40**, 7391–7394 (1989). doi: [10.1103/PhysRevB.40.7391](#); pmid: [9991153](#)
14. H. J. Schulz, Incommensurate antiferromagnetism in the two-dimensional Hubbard model. *Phys. Rev. Lett.* **64**, 1445–1448 (1990). doi: [10.1103/PhysRevLett.64.1445](#); pmid: [10041397](#)
15. K. Machida, Magnetism in La_2CuO_4 based compounds. *Physica C* **158**, 192–196 (1989). doi: [10.1016/0921-4534\(89\)90316-X](#)
16. T. Maier, M. Jarrell, T. Pruschke, M. H. Hettler, Quantum cluster theories. *Rev. Mod. Phys.* **77**, 1027–1080 (2005). doi: [10.1103/RevModPhys.77.1027](#)
17. A.-M. Tremblay, B. Kyung, D. Sénéchal, Pseudogap and high-temperature superconductivity from weak to strong coupling. Towards a quantitative theory (Review Article). *Low Temp. Phys.* **32**, 424–451 (2006). doi: [10.1063/1.2199446](#)
18. G. Kotliar *et al.*, Electronic structure calculations with dynamical mean-field theory. *Rev. Mod. Phys.* **78**, 865–951 (2006). doi: [10.1103/RevModPhys.78.865](#)
19. A. Macridin, M. Jarrell, T. Maier, P. R. C. Kent, E. D'Azevedo, Pseudogap and antiferromagnetic correlations in the Hubbard model. *Phys. Rev. Lett.* **97**, 036401 (2006). doi: [10.1103/PhysRevLett.97.036401](#); pmid: [16907520](#)
20. E. Gull, M. Ferrero, O. Parcollet, A. Georges, A. J. Millis, Momentum-space anisotropy and pseudogaps: A comparative cluster dynamical mean-field analysis of the doping-driven metal-insulator transition in the two-dimensional Hubbard model. *Phys. Rev. B Condens. Matter Mater. Phys.* **82**, 155101 (2010). doi: [10.1103/PhysRevB.82.155101](#)
21. O. Gunnarsson *et al.*, Fluctuation Diagnostics of the Electron Self-Energy: Origin of the Pseudogap Physics. *Phys. Rev. Lett.* **114**, 236402 (2015). doi: [10.1103/PhysRevLett.114.236402](#); pmid: [26196809](#)
22. W. Wu, M. Ferrero, A. Georges, E. Kozik, Controlling Feynman diagrammatic expansions: Physical nature of the pseudogap in the two-dimensional Hubbard model. *Phys. Rev. B* **96**, 041105 (R) (2017). doi: [10.1103/PhysRevB.96.041105](#)
23. F. Krien, P. Worm, P. Chalupa-Gantner, A. Toschi, K. Held, Explaining the pseudogap through damping and antidamping on the Fermi surface by imaginary spin scattering. *Commun. Phys.* **5**, 336 (2022). doi: [10.1038/s42005-022-01117-5](#)
24. Materials and methods are available as supplementary materials.
25. N. Prokof'ev, B. Svistunov, Fermi-polaron problem: Diagrammatic Monte Carlo method for divergent sign-alternating series. *Phys. Rev. B Condens. Matter Mater. Phys.* **77**, 020408 (2008). doi: [10.1103/PhysRevB.77.020408](#)

26. E. Kozik *et al.*, Diagrammatic Monte Carlo for correlated fermions. *Europhys. Lett.* **90**, 10004 (2010). doi: [10.1209/0295-5075/90/10004](https://doi.org/10.1209/0295-5075/90/10004)
27. K. Van Houcke *et al.*, Feynman diagrams versus Fermi-gas Feynman emulator. *Nat. Phys.* **8**, 366–370 (2012). doi: [10.1038/nphys2273](https://doi.org/10.1038/nphys2273)
28. R. Rossi, Determinant Diagrammatic Monte Carlo Algorithm in the Thermodynamic Limit. *Phys. Rev. Lett.* **119**, 045701 (2017). doi: [10.1103/PhysRevLett.119.045701](https://doi.org/10.1103/PhysRevLett.119.045701); pmid: [29341772](https://pubmed.ncbi.nlm.nih.gov/29341772/)
29. K. Chen, K. Haule, A combined variational and diagrammatic quantum Monte Carlo approach to the many-electron problem. *Nat. Commun.* **10**, 3725 (2019). doi: [10.1038/s41467-018-07882-8](https://doi.org/10.1038/s41467-018-07882-8); pmid: [30602773](https://pubmed.ncbi.nlm.nih.gov/30602773/)
30. F. Šimkovic IV *et al.*, Extended Crossover from a Fermi Liquid to a Quasiantiferromagnet in the Half-Filled 2D Hubbard Model. *Phys. Rev. Lett.* **124**, 017003 (2020). doi: [10.1103/PhysRevLett.124.017003](https://doi.org/10.1103/PhysRevLett.124.017003); pmid: [31976700](https://pubmed.ncbi.nlm.nih.gov/31976700/)
31. A. Georges, G. Kotliar, W. Krauth, M. J. Rozenberg, Dynamical mean-field theory of strongly correlated fermion systems and the limit of infinite dimensions. *Rev. Mod. Phys.* **68**, 13–125 (1996). doi: [10.1103/RevModPhys.68.13](https://doi.org/10.1103/RevModPhys.68.13)
32. E. Gull *et al.*, Continuous-time Monte Carlo methods for quantum impurity models. *Rev. Mod. Phys.* **83**, 349–404 (2011). doi: [10.1103/RevModPhys.83.349](https://doi.org/10.1103/RevModPhys.83.349)
33. A. N. Rubtsov, V. V. Savkin, A. I. Lichtenstein, Continuous-time quantum Monte Carlo method for fermions. *Phys. Rev. B Condens. Matter Mater. Phys.* **72**, 035122 (2005). doi: [10.1103/PhysRevB.72.035122](https://doi.org/10.1103/PhysRevB.72.035122)
34. Throughout this study, we did not perform numerical analytic continuations but rather based our study on a direct analysis of imaginary time/frequency Monte Carlo data.
35. Y. M. Vilk, A.-M. S. Tremblay, Non-Perturbative Many-Body Approach to the Hubbard Model and Single-Particle Pseudogap. *J. Phys. I* **7**, 1309–1368 (1997). doi: [10.1051/jpl.1997135](https://doi.org/10.1051/jpl.1997135)
36. T. A. Sedrakyan, A. V. Chubukov, Pseudogap in underdoped cuprates and spin-density-wave fluctuations. *Phys. Rev. B Condens. Matter Mater. Phys.* **81**, 174536 (2010). doi: [10.1103/PhysRevB.81.174536](https://doi.org/10.1103/PhysRevB.81.174536)
37. F. Šimkovic IV, R. Rossi, M. Ferrero, Two-dimensional Hubbard model at finite temperature: Weak, strong, and long correlation regimes. *Phys. Rev. Res.* **4**, 043201 (2022). doi: [10.1103/PhysRevResearch.4.043201](https://doi.org/10.1103/PhysRevResearch.4.043201)
38. E. W. Huang, C. B. Mendl, H.-C. Jiang, B. Moritz, T. P. Devereaux, Stripe order from the perspective of the Hubbard model. *NPJ Quantum Mater.* **3**, 22 (2018). doi: [10.1038/s41535-018-0097-0](https://doi.org/10.1038/s41535-018-0097-0)
39. P. Mai, S. Karakuzu, G. Balduzzi, S. Johnston, T. A. Maier, Intertwined spin, charge, and pair correlations in the two-dimensional Hubbard model in the thermodynamic limit. *Proc. Natl. Acad. Sci. U.S.A.* **119**, e2112806119 (2022). doi: [10.1073/pnas.2112806119](https://doi.org/10.1073/pnas.2112806119); pmid: [35140180](https://pubmed.ncbi.nlm.nih.gov/35140180/)
40. O. Parcollet, G. Biroli, G. Kotliar, Cluster dynamical mean field analysis of the mott transition. *Phys. Rev. Lett.* **92**, 226402 (2004). doi: [10.1103/PhysRevLett.92.226402](https://doi.org/10.1103/PhysRevLett.92.226402); pmid: [15245242](https://pubmed.ncbi.nlm.nih.gov/15245242/)
41. K. Haule, G. Kotliar, Strongly correlated superconductivity: A plaquette dynamical mean-field theory study. *Phys. Rev. B Condens. Matter Mater. Phys.* **76**, 104509 (2007). doi: [10.1103/PhysRevB.76.104509](https://doi.org/10.1103/PhysRevB.76.104509)
42. M. Ferrero *et al.*, Pseudogap opening and formation of Fermi arcs as an orbital-selective Mott transition in momentum space. *Phys. Rev. B Condens. Matter Mater. Phys.* **80**, 064501 (2009). doi: [10.1103/PhysRevB.80.064501](https://doi.org/10.1103/PhysRevB.80.064501)
43. T. Schäfer *et al.*, Tracking the Footprints of Spin Fluctuations: A MultiMethod, MultiMessenger Study of the Two-Dimensional Hubbard Model. *Phys. Rev. X* **11**, 011058 (2021). doi: [10.1103/PhysRevX.11.011058](https://doi.org/10.1103/PhysRevX.11.011058)
44. T. Schäfer, A. Toschi, How to read between the lines of electronic spectra: The diagnostics of fluctuations in strongly correlated electron systems. *J. Phys. Condens. Matter* **33**, 214001 (2021). doi: [10.1088/1361-648X/abeb44](https://doi.org/10.1088/1361-648X/abeb44); pmid: [33652424](https://pubmed.ncbi.nlm.nih.gov/33652424/)
45. L. Hedin, New Method for Calculating the One-Particle Green's Function with Application to the Electron-Gas Problem. *Phys. Rev.* **39** (3A), A796–A823 (1965). doi: [10.1103/PhysRev.39.A796](https://doi.org/10.1103/PhysRev.39.A796)
46. R. E. V. Profumo, C. Groth, L. Messio, O. Parcollet, X. Waintal, Quantum Monte Carlo for correlated out-of-equilibrium nanoelectronic devices. *Phys. Rev. B Condens. Matter Mater. Phys.* **91**, 245154 (2015). doi: [10.1103/PhysRevB.91.245154](https://doi.org/10.1103/PhysRevB.91.245154)
47. R. Rossi, F. Werner, N. Prokof'ev, B. Svistunov, Shifted-action expansion and applicability of dressed diagrammatic schemes. *Phys. Rev. B* **93**, 161102 (2016). doi: [10.1103/PhysRevB.93.161102](https://doi.org/10.1103/PhysRevB.93.161102)
48. R. Rossi, F. Šimkovic, M. Ferrero, Renormalized perturbation theory at large expansion orders. *Europhys. Lett.* **132**, 11001 (2020). doi: [10.1209/0295-5075/132/11001](https://doi.org/10.1209/0295-5075/132/11001)
49. C. Proust, L. Taillefer, The Remarkable Underlying Ground States of Cuprate Superconductors. *Annu. Rev. Condens. Matter Phys.* **10**, 409–429 (2019). doi: [10.1146/annurev-conmatphys-031218-013210](https://doi.org/10.1146/annurev-conmatphys-031218-013210)
50. S. Sorella, Systematically improvable mean-field variational ansatz for strongly correlated systems: Application to the Hubbard model. *Phys. Rev. B* **107**, 115133 (2023). doi: [10.1103/PhysRevB.107.115133](https://doi.org/10.1103/PhysRevB.107.115133)
51. M. Kitatani *et al.*, Optimizing Superconductivity: From Cuprates via Nickelates to Palladates. *Phys. Rev. Lett.* **130**, 166002 (2023). doi: [10.1103/PhysRevLett.130.166002](https://doi.org/10.1103/PhysRevLett.130.166002); pmid: [37154662](https://pubmed.ncbi.nlm.nih.gov/37154662/)
52. M. Qin *et al.*, Absence of Superconductivity in the Pure Two-Dimensional Hubbard Model. *Phys. Rev. X* **10**, 031016 (2020). doi: [10.1103/PhysRevX.10.031016](https://doi.org/10.1103/PhysRevX.10.031016)
53. B. Xiao, Y.-Y. He, A. Georges, S. Zhang, Temperature Dependence of Spin and Charge Orders in the Doped Two-Dimensional Hubbard Model. *Phys. Rev. X* **13**, 011007 (2023). doi: [10.1103/PhysRevX.13.011007](https://doi.org/10.1103/PhysRevX.13.011007)
54. A. V. Chubukov, Kohn-Luttinger effect and the instability of a two-dimensional repulsive Fermi liquid at $T=0$. *Phys. Rev. B Condens. Matter* **48**, 1097–1104 (1993). doi: [10.1103/PhysRevB.48.1097](https://doi.org/10.1103/PhysRevB.48.1097); pmid: [10007968](https://pubmed.ncbi.nlm.nih.gov/10007968/)
55. Y. Deng, E. Kozik, N. V. Prokof'ev, B. V. Svistunov, Emergent BCS regime of the two-dimensional fermionic Hubbard model: Ground-state phase diagram. *Europhys. Lett.* **110**, 57001 (2015). doi: [10.1209/0295-5075/110/57001](https://doi.org/10.1209/0295-5075/110/57001)
56. F. Šimkovic IV, Y. Deng, E. Kozik, Superfluid ground state phase diagram of the two-dimensional Hubbard model in the emergent Bardeen-Cooper-Schrieffer regime. *Phys. Rev. B* **104**, L020507 (2021). doi: [10.1103/PhysRevB.104.L020507](https://doi.org/10.1103/PhysRevB.104.L020507)
57. E. Gull, O. Parcollet, A. J. Millis, Superconductivity and the pseudogap in the two-dimensional Hubbard model. *Phys. Rev. Lett.* **110**, 216405 (2013). doi: [10.1103/PhysRevLett.110.216405](https://doi.org/10.1103/PhysRevLett.110.216405); pmid: [23745902](https://pubmed.ncbi.nlm.nih.gov/23745902/)
58. M. Kitatani, T. Schäfer, H. Aoki, K. Held, Why the critical temperature of high- T_c cuprate superconductors is so low: The importance of the dynamical vertex structure. *Phys. Rev. B* **99**, 041115 (2019). doi: [10.1103/PhysRevB.99.041115](https://doi.org/10.1103/PhysRevB.99.041115)
59. H. Xu, C.-M. Chung, M. Qin, U. Schollwöck, S. R. White, S. Zhang, Coexistence of superconductivity with partially filled stripes in the Hubbard model. *arXiv:2303.08376* [cond-mat.supr-con] (2023).
60. A. Moutenet, W. Wu, M. Ferrero, Determinant Monte Carlo algorithms for dynamical quantities in fermionic systems. *Phys. Rev. B* **97**, 085117 (2018). doi: [10.1103/PhysRevB.97.085117](https://doi.org/10.1103/PhysRevB.97.085117)
61. F. Šimkovic, E. Kozik, Determinant Monte Carlo for irreducible Feynman diagrams in the strongly correlated regime. *Phys. Rev. B* **100**, 121102(R) (2019). doi: [10.1103/PhysRevB.100.121102](https://doi.org/10.1103/PhysRevB.100.121102)
62. R. Rossi, Direct sampling of the self-energy with Connected Determinant Monte Carlo <https://arxiv.org/abs/1802.04743> (2018).
63. F. Šimkovic IV, M. Ferrero, Fast principal minor algorithms for diagrammatic Monte Carlo. *Phys. Rev. B* **105**, 125104 (2022). doi: [10.1103/PhysRevB.105.125104](https://doi.org/10.1103/PhysRevB.105.125104)
64. F. Šimkovic IV, R. Rossi, Many-Configuration Markov-Chain Monte Carlo. [arXiv:2102.05613](https://arxiv.org/abs/2102.05613) [physics.comp-ph] (2021).
65. G. Benfatto, A. Giuliani, V. Mastropietro, Fermi Liquid Behavior in the 2D Hubbard Model at Low Temperatures. *Ann. Henri Poincaré* **7**, 809–898 (2006). doi: [10.1007/s00023-006-0270-z](https://doi.org/10.1007/s00023-006-0270-z)
66. F. Šimkovic IV, R. Rossi, A. Georges, M. Ferrero, Data for: Origin and fate of the pseudogap in the doped Hubbard model, Zenodo (2024); <https://doi.org/10.5281/zenodo.11122566>.
67. R. Rossi, F. Šimkovic, FastFeynmanDiagrammatics/FastFeynmanDiagrammatics: v0.0.1, Zenodo (2024); <https://doi.org/10.5281/zenodo.12698824>.

ACKNOWLEDGMENTS

We are grateful to S. Sachdev, S. White, B. Xiao, and S. Zhang for insightful discussions. We also acknowledge fruitful discussions with S. Sorella and J. Zaanen, and we dedicate this article to their memory. **Funding:** This work was granted access to the HPC resources of TGCC and IDRIS under the allocations A0090510609 and A0110510609 attributed by GENCI (Grand Equipement National de Calcul Intensif). F.Š. and M.F. acknowledge the support of the Simons Foundation within the Many Electron Collaboration framework. The Flatiron Institute is a division of the Simons Foundation. **Author contributions:** All authors conceived the study. F.Š. and R.R. developed DiagMC simulation codes. F.Š. performed DiagMC calculations and data postprocessing. F.Š. performed DMFT calculations. M.F. performed DCA and CT-INT calculations. All authors contributed to the physical analysis of the results and to the writing of the manuscript. **Competing interests:** The authors declare that they have no competing interests. **Data and materials availability:** All data needed to reproduce the conclusions in this study are presented in the main text or the supplementary materials. Data presented in the figures, raw DiagMC, DMFT, DCA, and CT-INT data, as well as postprocessing scripts are deposited online at Zenodo (66). The diagrammatic Monte Carlo code is available at Zenodo (67). **License information:** Copyright © 2024 the authors, some rights reserved; exclusive licensee American Association for the Advancement of Science. No claim to original US government works. <https://www.science.org/about/science-licenses-journal-article-reuse>

SUPPLEMENTARY MATERIALS

science.org/doi/10.1126/science.ade9194

Supplementary Text
Figs. S1 to S20
References (68–70)

Submitted 19 September 2022; accepted 9 July 2024
[10.1126/science.ade9194](https://doi.org/10.1126/science.ade9194)